ACS NANO

www.acsnano.org

ARTICLE

Quantifying Dynamic Changes of Oxygen Nonstoichiometry and Formation of Surface Phases of $SrCoO_x$ Electrocatalysts by *Operando* Characterizations

Yang Hu, Luhan Wei, Haowen Chen, Zihan Xu, Andrey Shavorskiy, Christoph Baeumer,* and Qiyang Lu*

Cite This: *ACS Nano* 2025, 19, 13999−14009

Read Online

ACCESS | Metrics & More | Article Recommendations | Supporting Information

ABSTRACT: **Perovskite electrocatalysts like strontium cobaltite ($SrCoO_x$, denoted as SCO) experience dynamic changes in both surface and bulk during the oxygen evolution reaction (OER), rather than remaining static. This dynamic, electrochemically driven evolution in composition, structure, and ionic defects (*e.g.*, oxygen vacancies) can strongly impact the OER activity and stability. Yet, the current lack of quantitative information on these processes impedes a precise and predictive evaluation of the individual and combined effect of both bulk and surface transformations. Here, using epitaxial SCO thin films as a model system, we demonstrate that SCO is a bulk and surface redox-active OER electrocatalyst that undergoes a bulk phase transition via electrochemically induced oxygen intercalation, as well as a surface phase transition toward Co (oxy-)hydroxide. Specifically, applying a suite of *operando* and *ex situ* characterization we established a reliable relationship between oxygen nonstoichiometry, optical density, and conductivity as a function of applied potentials. We further accurately quantify the evolution of oxygen stoichiometry in the SCO bulk and the thickness of the formed surface secondary phase. Our work provides a reliable and generalizable workflow and *operando* characterization toolbox for quantitative assessment of surface and bulk transformations in oxygen-deficient perovskite electrocatalysts.**

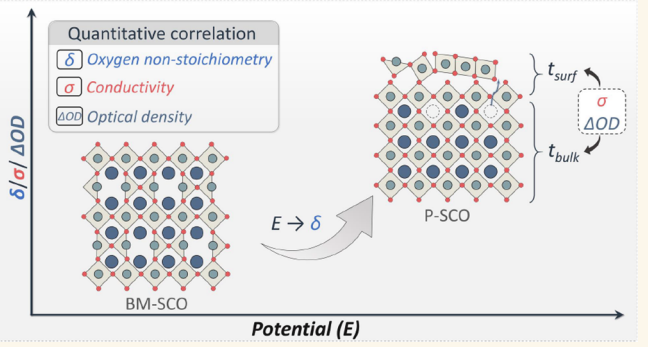

KEYWORDS: *perovskite oxides, thin film, oxygen evolution reaction, phase transitions, operando characterization*

INTRODUCTION

Perovskite-type oxides (ABO_3) have emerged as one of the most promising electrocatalyst candidates for catalyzing the oxygen evolution reaction (OER) because of the tunable chemical compositions and electronic structures through modulating the A-site and B-site cations, as well as precisely controlled ionic defect concentrations.[1−5] Observations in recent years have shown that these oxide electrocatalysts undergo dynamic changes during OER. These changes affect the chemical composition and electronic structure of the both surface and bulk of electrocatalysts and depend on the applied current and potential load.[6] This revelation contrasts sharply with the conventional view that assumes a static composition and structure of the bulk solid electrocatalyst.[7−9] Importantly, the dynamic surface and bulk properties rather than the static as-prepared case determine the OER performance. However, the current relevant literature is mostly qualitative, lacking quantitative insights. This absence of quantitative assessment hampers the precise evaluation and predictive utilization of both individual and combined effects of dynamic bulk compositional changes and surface structural evolution on catalytic activity.

First, in the bulk, ionic defects (most prominently in the form of oxygen vacancies) in perovskite oxides and overall changes in composition directly impact electronic structure

Received: December 14, 2024
Revised: March 29, 2025
Accepted: March 31, 2025
Published: April 7, 2025

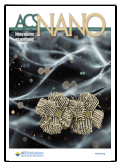

https://doi.org/10.1021/acsnano.4c18105
ACS Nano 2025, 19, 13999−14009

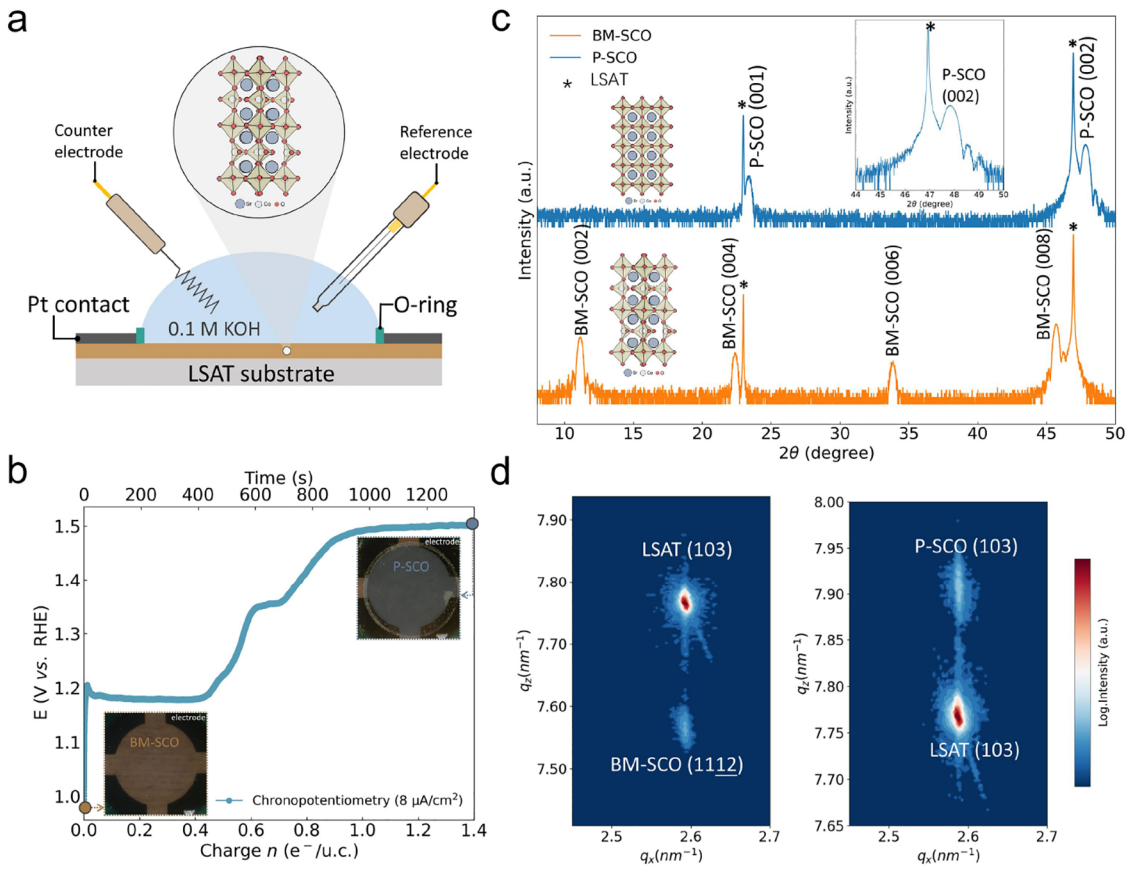

Figure 1. Phase transition of SCO during electrochemical reaction. (a) Schematic diagram of the three-electrode setup for electrochemical measurement on epitaxial thin film. (b) Chronopotentiometry (CP) measurement on as-prepared brownmillerite phase $SrCoO_{2.5}$ (BM-SCO). The bottom *x*-axis represents the transferred charge *n* per formula unit starting material. The inset shows optical images of the sample before and after the test. (c) High-resolution X-ray diffraction of the BM-SCO (pristine) and P-SCO (post-CP). Inset: 2θ-ω scan of the (002) diffraction peak of P-SCO. (d) Reciprocal space mapping of BM-SCO and P-SCO.

and active sites. Various studies have demonstrated that oxygen vacancies in perovskite oxides can be controlled by external electrochemical driving forces.[10−12] Especially the more recent findings of oxygen vacancy concentration control at room temperature in aqueous electrochemistry mandate careful consideration and especially quantification of bulk defect levels during dynamic changes of perovskite electrocatalysts under OER conditions. In high-temperature electrochemical reactions, the role of defect concentration, usually quantitatively understood by using so-called Brouwer diagrams,[13] is explicitly considered when modeling reaction kinetics. Defect concentration is directly related to the oxygen nonstoichiometry, and can be finely manipulated either chemically or electrochemically.[13−15] In contrast, the understanding of oxygen defects at room temperature under aqueous electrochemical conditions is still evolving, making it crucial to establish a clear quantitative relationship between defect concentration (*i.e.*, oxygen nonstoichiometry) and applied potential.

Second, at the catalyst surface, the formation of transition metal oxyhydroxides is widely observed at the solid/electrolyte interfaces of the perovskite electrocatalyst family.[2,9,16,17] The formed surface secondary phase has been experimentally evidenced as surface-active species for catalyzing OER (*e.g.*, NiO_xH_y on $LaNiO_{3-\delta}$,[2] CoO(OH) on $La_{0.6}Sr_{0.4}CoO_{3-\delta}$[9]). Again, these observations were so far mainly limited to phenomenological discussions without quantification. Moreover, post-mortem characterization was often used in the literature to reveal the formation of oxy-hydroxide at surfaces,[18,19] but this approach cannot elucidate the dynamic surface structure evolution during the reaction. Therefore, there is an urgent need to develop *operando* techniques to shed light on and quantify the surface and bulk changes of perovskite oxide electrocatalysts under reaction conditions.

In this work, we selected epitaxial single-crystalline $SrCoO_{2.5+\delta}$ (SCO, oxygen nonstoichiometry is denoted by δ) thin films as a well-defined model system to investigate dynamic transformations. The well-controlled geometry, composition, and crystal facets of the SCO thin films, and the previously observed coexistence of pronounced surface and bulk transformations with applied potential make SCO thin films an ideal starting point for rationally designed *operando* characterization techniques. The dynamic changes of oxygen nonstoichiometry in SCO were precisely quantified as a function of applied potentials through coulometric titration. The evolution of the electronic conductivity of SCO was tracked by *operando* conductivity measurement, which revealed a direct correlation with the bulk oxygen nonstoichiometry change. Surface-sensitive characterization techniques confirmed a surface phase transformation toward a cobalt (oxy-)hydroxide layer and identified the electrochemically induced Sr leaching as the driver for the formation of the new surface phase. Importantly, we successfully quantified the thickness of the formed cobalt oxyhydroxides surface secondary phase

https://doi.org/10.1021/acsnano.4c18105
ACS Nano 2025, 19, 13999−14009

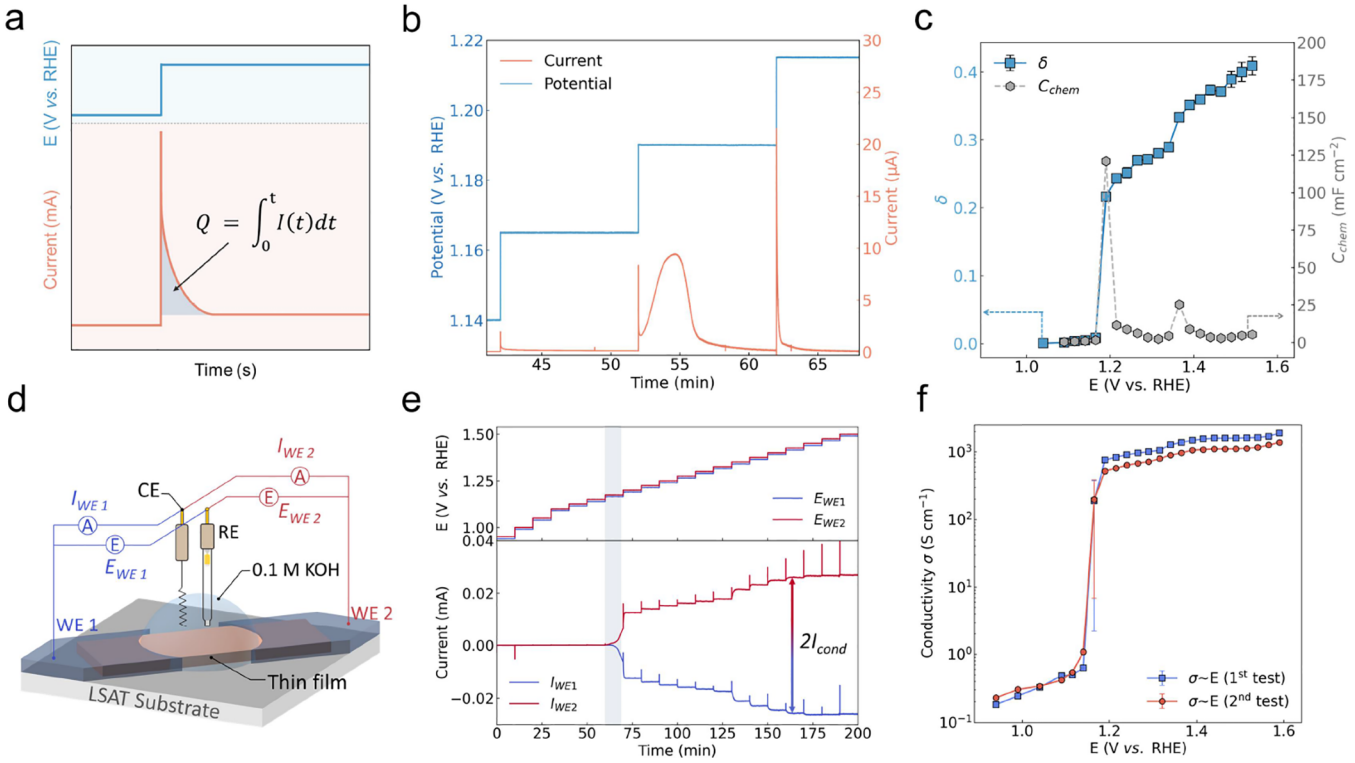

Figure 2. Oxygen nonstoichiometry and conductivity in SCO as a function of applied anodic potentials. (a) Schematic *I*−*t* plot under a constant potential, showing the procedure of integrating passed charges. (b) Section of the chronoamperometry measurement showing different constant anodic potentials (blue) with the current responses (red). (c) The changes of oxygen nonstoichiometry (δ) and chemical capacitance (C_{chem}) at different applied anodic potentials. (d) Schematic of the dual-working-electrode experimental setup for *operando* conductivity measurement. An O-ring is used to keep the contact electrode away from the electrolyte. (e) The current response of WE1 and WE2 under potential step voltammetry during the first test. (f) The measured conductivity of SCO at different applied potentials in two test cycles. Error bars indicate the deviation of measured currents under a nonsteady state of the sample (marked by the gray shading in Figure 2e).

under OER conditions by various methods, including *operando* conductivity measurement, scanning transmission electron microscopy, and *operando* UV−vis spectroelectrochemistry. The results from multiple techniques were found to be quantitatively consistent, establishing a reliable relationship between optical density, conductivity, and oxygen nonstoichiometry as a function of applied potentials. This marks a notable advance over previous studies, which were limited to qualitative observations. While the precise quantification of bulk oxygen nonstoichiometry and surface secondary phase was demonstrated using SCO as a proof of principle, we believe that our proposed *operando* techniques toolbox is generalizable to other OER electrocatalyst thin films. It thus enhances quantitative understanding of both bulk and surface dynamic evolution and phase transitions, and important ingredient for the design of OER electrocatalysts.

RESULTS AND DISCUSSION

Oxygen Intercalation in Strontium Cobaltite from BM-SCO to P-SCO via an Electrochemical Reaction. Brownmillerite phase $SrCoO_{2.5}$ (BM-SCO) thin films with a thickness of ∼25 nm were epitaxially grown on (001)-oriented LSAT substrates using pulsed laser deposition (PLD) (see details in Methods). We conducted electrochemical measurements employing the thin film as a working electrode in a three-electrode setup (Figure 1a). We carried out chronopotentiometry (CP) measurements with a constant current density of 8 μA cm^{-2} on as-prepared BM-SCO in 0.1 M KOH. Figure 1b shows the electrochemical response of SCO during the oxidation process. Since we applied a constant current, we can calculate the transferred charge easily, which is then normalized to the volume of the starting BM-SCO. We observed the appearance of multiple potential plateaus in the *E*−*t* (voltage−time) curve, indicating the formation of multiple SCO intermediate phases with different oxygen contents.[20,21]

Additionally, we found that the sample shows varying optical colors from brownish to gray before and after the CP test, respectively (Figure 1b inset), further indicating the presence of bulk transformation in SCO. To provide direct evidence of structural changes in SCO, we performed high-resolution X-ray diffraction (HRXRD) on samples before and after the CP test, as shown in Figure 1c. The half-order (002) peak, considered as the fingerprint of the BM phase due to its origin in the layered oxygen vacancy structure,[22] disappeared after electrochemical oxidation and new diffraction peaks of perovskite phase $SrCoO_{2.5+\delta}$ (P-SCO) were present, suggesting that the film was transformed from BM phase to P phase. The clear Laue fringes in the (002) diffraction peak of P-SCO (∼47.8°) and the rocking curve measurement (Figure S1) indicate the high crystalline quality of the film throughout the topotactic phase transition. Reciprocal space mapping (RSM) further confirms the formation of the perovskite phase through the dramatic change of out-of-plane lattice parameter from 3.97 Å (BM-SCO) to 3.80 Å (P-SCO). The film remained fully strained to the substrate, as evident from the in-plane lattice parameter (Figure 1d). Thus, our electrochemical results and

https://doi.org/10.1021/acsnano.4c18105
ACS Nano 2025, 19, 13999−14009

structure characterization corroborate that $SrCoO_{2.5+\delta}$ is a bulk-redox OER electrocatalyst, going through the BM → P phase transition via electrochemically induced oxygen intercalation.

Dynamic Bulk Transformation in SCO: Oxygen Nonstoichiometry Quantification and *Operando* Conductivity Measurement. Since we have confirmed that the SCO electrocatalyst undergoes a phase transition from BM to P during the OER test, it is evident that the oxygen content in SCO changes significantly as the anodic potential increases during the electrocatalytic reaction. This varying oxygen content, or different oxygen vacancy concentrations in SCO, will induce changes in the electronic structure, thereby greatly influencing the electrocatalytic activity of SCO.[23,24] To quantitatively understand how the oxygen content in SCO electrocatalysts varies with the applied electrochemical potential, we performed a coulometric titration method to quantify the change of oxygen nonstoichiometry (δ) in SCO from $SrCoO_{2.5}$ to $SrCoO_{2.5+\delta}$ as a function of applied potential (i.e., the oxygen chemical potential). From a defect chemical perspective, this is equivalent to deriving a partial Brouwer diagram. Figure 2a shows the example of calculating transferred charges (Q) in SCO from an $I-t$ plot under a certain applied potential. The δ is calculated using the equation below:

$$\delta = \frac{QV_{\mathrm{u.c.}}}{neV_{\mathrm{film}}} \tag{1}$$

where Q represents the number of transferred charges, n denotes the charge per intercalated oxygen ion (in this case, $n = 2$), e is the elementary charge, and $V_{\mathrm{u.c.}}$ represents the volume of the unit cell of SCO. To calculate the $V_{\mathrm{u.c.}}$, the out-of-plane lattice parameter of as-prepared BM-SCO was used from HRXRD data in Figure S1 and we assume that the in-plane lattice parameter remains unchanged during the phase transition process based on the RSM result from Figure 1d. V_{film} is the volume of the thin film that is exposed to the electrolyte ($V_{\mathrm{film}} = \pi \times r^2 \times t_{\mathrm{film}}$, where r is the inner radius of O-ring and t_{film} represents the film thickness). Figure 2b shows a section of the $I-t$ plot of the chronoamperometry measurement. At a potential step, one generally expects a current peak with exponential decay due to the capacitive charging of the electrical double layer. The transient current response under 1.19 V vs reversible hydrogen electrode (denoted as RHE, all the potentials in this work are referenced to RHE) did not exponentially decrease with elapsed time, instead showing a pronounced peak shape, indicating an oxygen intercalation process. This phenomenon suggests a phase transition occurring at this potential, similar to the electrochemical response previously reported on Li_xFePO_4.[25] To rule out the contribution of electrochemical double-layer capacitance (denoted as C_{EDL}) on the calculated δ, we compared the values of the chemical capacitance (denoted as C_{chem}), a measure of the capability of chemical charge storage of a material, and estimated oxide C_{EDL} (see details in Supporting Note 1 and Figure S2). The contribution of C_{EDL} is negligible and the integrated Q is attributed to C_{chem}, which comes from the change in oxygen content. We further calculated the δ as a function of applied anodic potential on SCO and plotted it in Figure 2c. As the applied potential increases from OCV to 1.165 V, the variation of δ is small, indicating that the oxygen stoichiometry of SCO remains close to 2.5. However, when the applied potential reaches 1.19 V, δ significantly increases, suggesting the occurrence of the phase transition. At this potential, more oxygen is incorporated into the lattice, occupying the structural oxygen vacancies of the BM phase. This observation aligns with the observed appearance of the first plateau in Figure 1c. The assigned δ is around 0.25, which is consistent with the known reported intermediate phase of $SrCoO_{2.75}$,[21,26] further validating the results of the coulometric titration method for quantifying the δ as a function of applied potentials. Furthermore, with a continuous increase in the applied anodic potential, we observe another prominent increase in δ at 1.365 V. This means that the oxygen vacancy concentration in SCO still decreases with increasing potentials and the threshold potential here is also consistent with the response potential of the second plateau observed in Figure 1c. We found that the SCO as an OER electrocatalyst will accommodate a higher δ (i.e., lower oxygen vacancy concentration) when increasing potentials compared with the pristine sample.

The changes in oxygen nonstoichiometry can alter the intrinsic electronic structure of the electrocatalysts, particularly its conductivity, which is also linked to the activity of electrocatalysts. To gain more insights into the transformations induced by electrochemical reactions, we conducted an operando conductivity measurement to track dynamic changes in the SCO conductivity with varying applied potentials. As depicted in Figure 2d, *operando* conductivity tests were conducted in 0.1 M KOH by applying step potentials to two individual working electrodes (denoted as WE1 and WE2) simultaneously, while maintaining a specific potential offset between these two electrodes to drive electrical conduction in SCO (see details in methods). Typically, the extracted difference in response currents between the two electrodes is therefore twice the conductance current ($2I_{\mathrm{cond}}$, marked with an arrow). Figure 2e shows a section of the current response of WE1 and WE2 under potential step voltammetry during the first test. We observed a pronounced change in the response currents at a range from 1.165 to 1.190 V, indicating an increase in conduction current (decrease in SCO resistance). That means the BM → P phase transition is accompanied by a semiconductor-to-metal transition. For a more quantitative comparison, we further summarized the SCO conductance as a function of applied potentials, as shown in Figure 2f. A detailed discussion of the conductance derivation is provided in Supporting Note 2. We observe a similar trend as for the SCO oxygen nonstoichiometry with applied potentials. Furthermore, the measured conductance of P-SCO is 4 orders of magnitude higher than the BM-SCO, which is in agreement with previous reports,[10,21] further validating this *operando* conductivity measurement method.

To identify any changes after applying cyclic OER potentials, we repeated the potential step voltammetry measurement from 0.94 to 1.59 V (Figure 2f). In both cycles, the conductance of SCO shows a four-order magnitude increase with increasing applied potentials. However, a decrease in conductance was noted during the second test, with a ~24% decrease in conductance under higher anodic potentials compared to the first test. As conductivity is an intrinsic property of the material, we expect that a surface transition toward a poorly conducting surface phase with increasing thickness can account for the decreased conductance in the second test, which is presumably Co (oxy)hydroxide,[9] a point to which we will return later. Considering the comparably low conductivity of cobalt

https://doi.org/10.1021/acsnano.4c18105
ACS Nano 2025, 19, 13999−14009

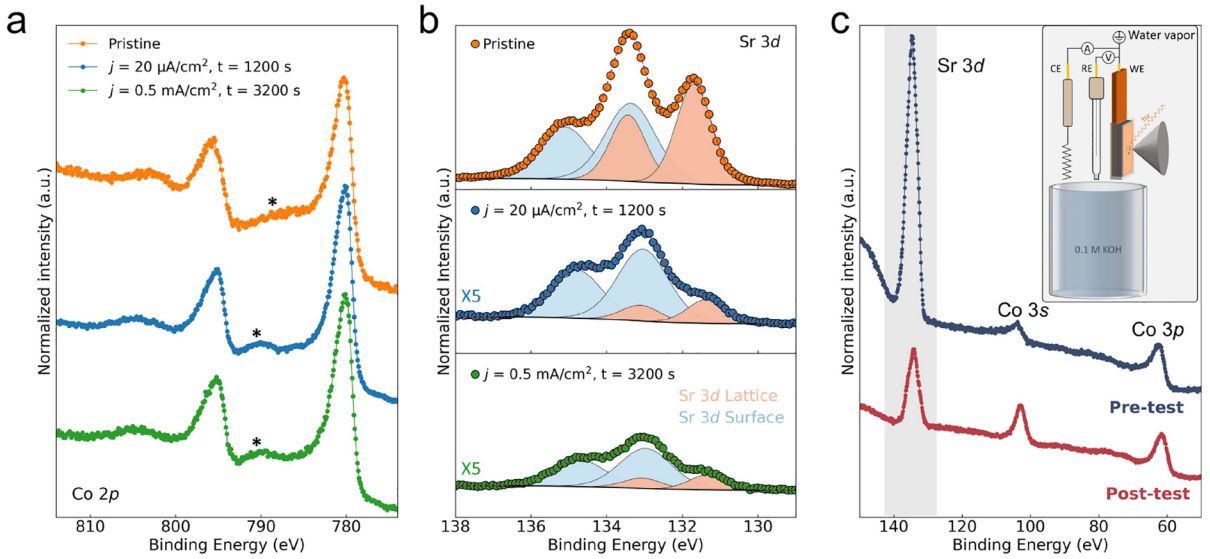

Figure 3. X-ray photoelectron spectroscopy (XPS) analysis for sample surface composition. (a) Co 2*p* and (b) Sr 3*d* normalized to the Co 2*p* area. (c) *In situ* ambient-pressure X-ray photoelectron spectroscopy (APXPS) of SCO. Comparison of Sr 3*d*, Co 3*s*, and Co 3*p* spectra before and after the potential step voltammetry test, normalized to the Co 3*p* area. The spectra were collected under equilibrium water vapor conditions at 10 °C (~12 mbar). The inset shows the used electrochemical *in situ* APXPS experimental configuration.

oxyhydroxide[27,28] and the sample thickness data from X-ray reflectivity measurements post second test (Figure S3 and Supporting Note 2), we could approximately derive the thickness of the formed surface phase (denoted as t_{surf}) using the *operando* conductivity measurement, arriving at a t_{surf} of 5.0 ± 0.1 nm while the bulk thickness of SCO (t_{bulk}) is 15.9 ± 0.1 nm. We thus found that *operando* conductivity measurement can serve dual purposes. Our method can both identify the bulk phase transition of SCO electrocatalyst during the electrochemical reaction by establishing a quantitative σ–E relationship and further enables the estimation of the thickness of the cobalt oxyhydroxide layer formed on the surface.

Surface Transformation in SCO: Electrochemically Induced Strontium Leaching Process in SCO. To investigate the changes in chemical composition on the surface of SCO electrocatalysts, we performed surface-sensitive X-ray photoelectron spectroscopy (XPS) to characterize the sample surfaces. Two out of three thin film samples grown from the same batch were tested under two different chronopotentiometry conditions (current density j = 20 μA/cm^2 and hold over 1200 s to yield the low passed charge, denoted as "low current density"; current density j = 0.5 mA/cm^2 and hold over 3200 s to yield the high passed charge, denoted as "high current density") and the third served as the pristine state comparison. Figure 3a shows the Co 2*p* spectra of SCO samples under various states, which are collected under vacuum. Compared to the pristine state, negligible change was observed in the Co $2p_{3/2}$ peak position (with the binding energy of ~780.2 eV) and shape of the post-test samples, whereas a satellite peak showed a significant binding energy shift from ~787 eV (pristine state) to ~790 eV (two operated states). This apparent satellite peak (marked with "*") toward high binding energy indicates an oxidation state of Co^{3+} in the surface phase after OER, which is consistent with recent reports for cobalt-based OER electrocatalysts.[9,29−31]

Figure 3b shows that the Sr 3*d* spectra were deconvoluted into two groups of Sr $3d_{5/2}$ and $3d_{3/2}$ peaks, corresponding to two chemical environments of Sr: the surface component (high binding energy, highlighted in blue) and the SCO lattice component (low binding energy, highlighted in orange). To compare the Sr/Co ratio of samples, the intensity of the Sr 3*d* spectra was normalized to the Co 2*p* area. The high Sr/Co ratio of the pristine sample suggests that the segregated Sr cations formed a secondary phase on the SCO surface (Figure S4), which is widely observed in Sr-containing perovskite oxides.[32,33] Then, we observed a dramatic decrease in the Sr/Co ratio after the CP test holding at a low current, indicating a process of strontium leaching under a given condition. A similar decrease was noted on the sample operated at a high current density. Regarding the peak shape, especially the contribution of the Sr 3*d* bulk decreases compared to the pristine state. To further rule out the potential effects of surface contamination and chemical state changes in *ex situ* tests, we conducted an *in situ* ambient-pressure X-ray photoelectron spectroscopy (APXPS) experiment to analyze the evolution of the surface chemical composition of SCO. As shown in Figure 3c, we collected XPS spectra before and after the electrochemical test, with the post-test spectra obtained after applying the OER potential. The intensity of the Sr 3*d* spectra was normalized to the Co 3*p* area. We observed a similar decreasing trend in Sr, further confirming the existence of a strontium leaching process on SCO during the electrochemical test. We suggest that the observed XPS trends are caused by the formation of oxyhydroxide-like surface phases, which are similar for both operating conditions.

Structure Observations of Surface and Bulk in Post-test SCO Electrocatalyst. To gain further insight into the surface and bulk structures of SCO after the electrochemical reaction, we performed scanning transmission electron microscopy (STEM) imaging to analyze the structure and chemical compositions of the sample after electrochemical oxidation. Two potential step voltammetry measurements (OCV to 1.59 V) were conducted on the as-prepared sample, with an increment of 100 mV and a 10-min hold at each potential step. Once the last measurement stopped at the final high potentials (1.59 V), we removed the sample from the

https://doi.org/10.1021/acsnano.4c18105
ACS Nano 2025, 19, 13999−14009

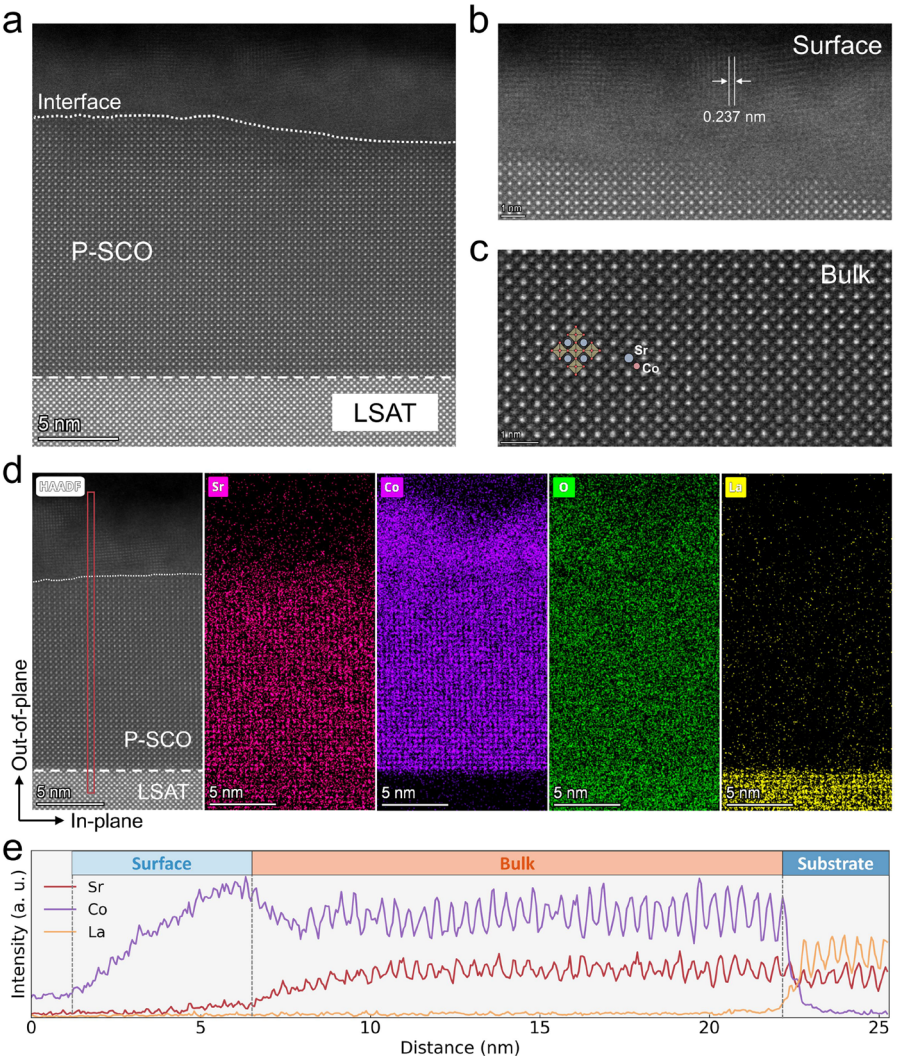

Figure 4. Structure characterization of the post-OER sample. (a) HAADF-STEM images of SCO after two cycles test. (b,c) Magnified HAADF-STEM images of surface and bulk area in (a). (d) Energy-dispersive X-ray spectroscopy (EDS) distribution of thin film and LSAT substrate. The dotted lines are guides to the eye to show the interface. (e) Line profile of elemental distribution from EDS mapping, extracted from the red marker in (d).

electrochemical cell. Lamella preparation and STEM imaging were performed on the same day, aiming to avoid potential post-experiment aging or relaxation. The cross-sectional high-angle annular dark field (HAADF) image reveals the atomic structure of the post-test SCO (Figure 4a). We find a highly crystalline phase in the bulk alongside an amorphous or low crystallinity phase at the film surface, both of which correspond well with the XRD and conductivity results discussed above. The surface layer exhibits periodic atomic structures in a small portion of the region observed at higher magnification (Figure 4b,c), where we measured the interplanar spacing to be 0.237 nm, corresponding to the $\{10\bar{1}0\}$ planes of CoOOH.[34] Interestingly, we did not observe the formation of cracks or amorphization in the bulk of SCO thin films as reported in a recent study by Bosse *et al.*[8] One possible reason for the difference is that our SCO thin films were grown on LSAT substrates, which has a smaller lattice mismatch with P-SCO compared with the thin films used in the study by Bosse *et al.*[8]

This observation is in line with the suspected formation of a cobalt oxyhydroxide-like phase on the SCO surface under OER conditions, deduced from the *operando* conductivity and the *ex situ* XPS measurements. Moreover, Figure 4c shows the well-defined perovskite structure in the bulk phase, further confirming the existence of BM → P phase transition in the SCO electrocatalyst bulk. Next, we conducted the energy-dispersive X-ray spectroscopy (EDS) on the thin film and substrate to obtain the distribution of chemical compositions, as shown in Figure 4d. We found that the concentration of Sr on the surface is markedly/substantially lower than that of the bulk, alongside a distinct Co enrichment at the surface. It is evident that the surface of SCO thin film undergoes the Sr leaching process and cobalt oxyhydroxide formation during OER conditions, strongly supporting the aforementioned expectation regarding the cause of the conductivity decrease and the XPS results. Accordingly, we suggest that the cobalt oxyhydroxide formation is the result of Sr leaching and cobalt reconstruction.[35] Further analysis was conducted by plotting line profiles of EDS composition in the vertical direction, as shown in Figure 4e. The spatial distribution of the three cations (Sr, Co, and La) in Figure 4e and measured TEM cross-section images (Figures S5 and S6) in 10 different locations enable us to determine the average thickness of the

https://doi.org/10.1021/acsnano.4c18105
ACS Nano 2025, 19, 13999−14009

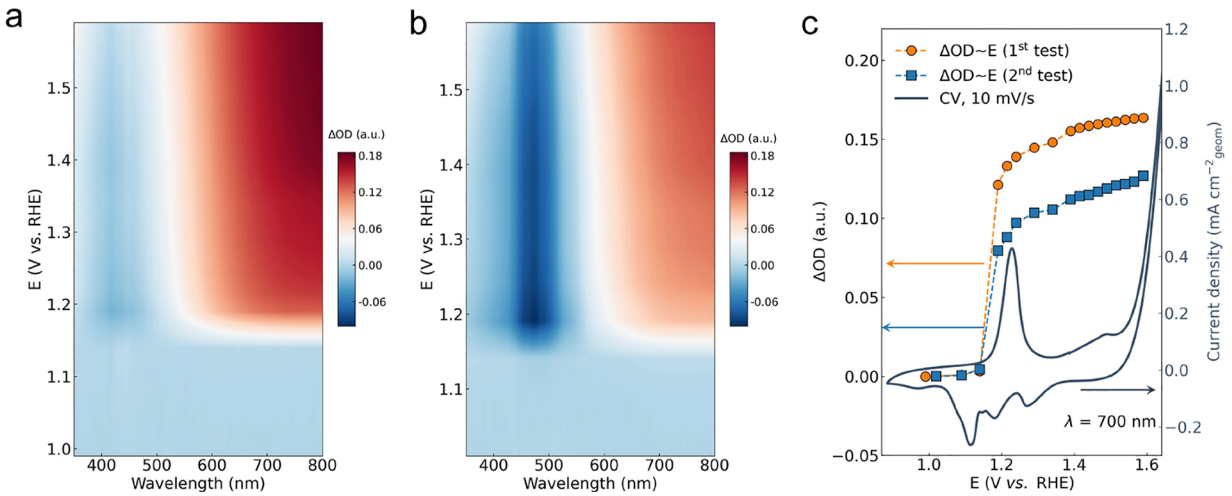

Figure 5. *Operando* UV−vis spectra as a function of applied potentials for SCO in 0.1 M KOH. (a) First potential step voltammetry test. (b) Second potential step voltammetry test. (c) Extracted optical density (OD) changes at λ = 700 nm as a function of the applied potential. The right *y*-axis shows the current density from cyclic voltammetry of SCO at 10 mV/s.

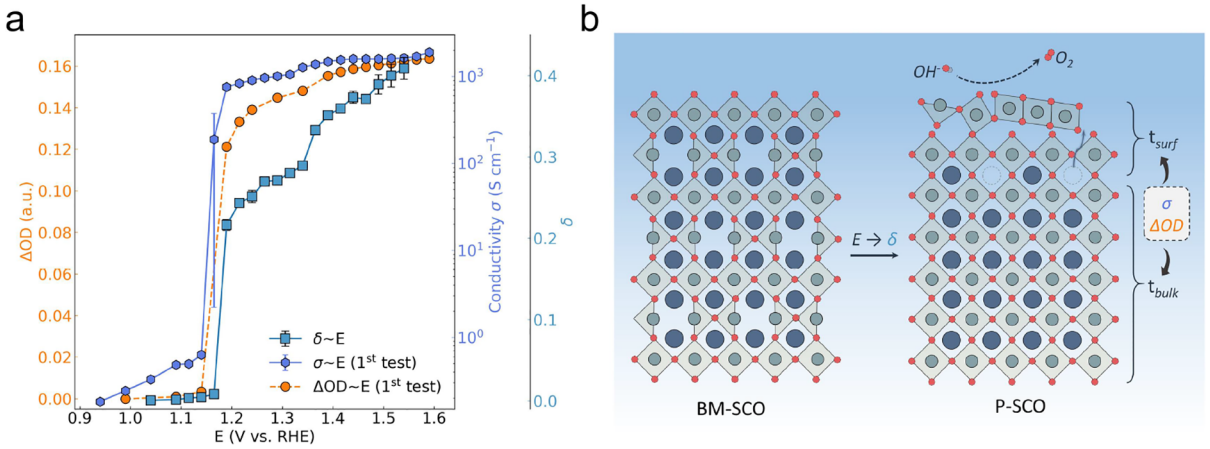

Figure 6. (a) Summarizing the relationship between the optical density change (**ΔOD**), conductivity (σ), and δ in SCO electrocatalyst as a function of applied potentials. (b) Schematic diagram of investigating surface and bulk phase transitions at the $SrCoO_x$ through *operando* techniques.

surface (~5.4 ± 0.6 nm) and bulk phases (~16.0 ± 1.2 nm) in the thin film. We also noticed the inhomogeneous thickness of the tested sample, which we suggest is linked to the strontium leaching process. Nevertheless, these values are nearly identical to what we obtained through the conductivity analysis, validating our approach of quantifying the thickness of surface and bulk phases in the electrocatalyst using *operando* conductivity measurements.

Probing the Surface and Bulk Phase Transitions of SCO during OER Using *Operando* UV−Vis Spectroscopy. Beyond using electrical properties to quantify the formed surface phase thickness, we also use optical properties for gaining further insights, which diversify our methods and offer cross-validation with the aforementioned conductivity measurements, thus improving the reliability and accuracy of the results. The results from the *operando* UV−vis spectroscopy, as we will show in the following, quantitatively agree and further corroborate our findings above from operando conductance measurement and *ex situ* characterizations. Figure 5a,b shows the correlation between the optical density change (ΔOD) and applied potentials across the entire wavelength range for two consecutive measurements. We observed variations in optical density across the applied potential range (from OCV to 1.59 V), most notable at λ = 700 nm, indicating that the ΔOD at this wavelength provides the optical information for the sample. The correlation of ΔOD at λ = 700 nm with increasing potentials with the characteristic redox features in cyclic voltammetry (CV) is shown in Figure 5c. We note a pronounced increase in ΔOD at 1.19 and 1.39 V, aligning with the observed redox features in the CV plot (Figure 5c) as well as in Figures 1 and 2. In the second potential step voltammetry measurement, we observed a lower ΔOD from 1.19 to 1.59 V compared to the first potential step voltammetry measurement. This indicates that the species contributing to optical density vary. We assume that the main contributions stem from bulk BM-SCO at low potential, bulk P-SCO at high potential, and a variable contribution of the surface layer, in which the oxygen and hydrogen composition of CoO_xH_y as well as the surface layer thickness may depend on the applied potential and cycles. Furthermore, we found that the potential corresponding to the onset of ΔOD change aligns with the aforementioned CP measurement (Figure 1) and the conductance measurement (Figure 2), suggesting a consistent behavior across different measurement techniques. To extract

https://doi.org/10.1021/acsnano.4c18105
ACS Nano 2025, 19, 13999−14009

more information about the surface phase from optical density data, we performed *operando* spectroelectrochemical testing on electrodeposited cobalt hydroxide (CoO_xH_y) thin films to obtain the spectral response of CoO_xH_y electrocatalyst as a reference (Figure S8). Subsequently, we quantitatively determined the extinction coefficients for CoO_xH_y and P-SCO, respectively (see details in Supporting Notes 3, 4, and Figure S9). This analysis enabled us to estimate the thicknesses of the surface (4.3 ± 0.7 nm) and bulk phases (17.2 ± 0.7 nm) formed after the second potential step voltammetry measurement. The UV−vis results are quantitatively consistent with those obtained from the conductivity and STEM analyses. Our findings confirm the applicability of *operando* UV−vis spectroelectrochemistry in detecting the formed surface layer on electrocatalysts under operation conditions.

The established quantitative relationships of physical properties (such as optical density ΔOD and conductivity σ) as well as oxygen nonstoichiometry δ as a function of potential E are illustrated in Figure 6a. The quantitatively consistent trends observed among these parameters with increasing applied potentials emphasize our capability to effectively establish quantitative ΔOD (and σ, δ) ∼ E correlations through the combination of the methods we discussed. The three quantities are all dependent on E and exhibit a sharp increase at the phase transition potential. This one-to-one correspondence of physical and chemical properties with oxygen nonstoichiometry will aid in constructing a complete Brouwer diagram for the room-temperature defect chemistry of perovskite electrocatalysts. This, in turn, will enhance our understanding of the role of oxygen vacancies in the context of room-temperature electrocatalysis. Additionally, during electrochemical cycling tests, we observed both surface and bulk phase transitions at the SCO (Figure 6b). The δ change with applied potentials was precisely quantified in SCO bulk ($E \rightarrow \delta$). Meanwhile, the SCO surface becomes depleted due to Sr leaching, and a cobalt (oxy)hydroxide layer forms at the surface under OER conditions. We successfully quantified the thickness of the formed surface layer and bulk after electrochemical tests through $E \rightarrow \sigma$ and $E \rightarrow$ ΔOD obtained from *operando* measurements. Given that cobalt (oxy)-hydroxides have been reported to actively catalyze the OER,[9,16,36] the proposed *operando* techniques for quantifying the formation of (oxy)hydroxides on the catalyst surface are particularly valuable. These techniques lay the foundation for future studies to differentiate the effects of surface and bulk changes on the OER activity, thereby deepening our understanding of the dynamic solid/liquid interface behavior in perovskite oxide OER catalysts.

CONCLUSIONS

In summary, we utilized epitaxial single-crystal $SrCoO_x$ thin films as a model system to explore dynamic surface and bulk phase transitions at the $SrCoO_x$. We experimentally found that $SrCoO_{3-x}$ acts as a bulk-redox OER electrocatalyst, undergoing the brownmillerite to perovskite phase transition through electrochemically induced oxygen intercalation. By employing coulometric titration, we quantitatively assessed the oxygen nonstoichiometry in the SCO electrocatalyst as a function of applied potential. A pronounced decrease in oxygen vacancy concentration within the bulk catalyst under applied anodic potentials challenges the concept of "frozen" point defect concentration in oxides at room temperature. Correspondingly, the intrinsic conductivity of SCO, determined through *operando* conductivity measurements, demonstrates a remarkable increase by 4 orders of magnitude with increasing applied potentials, underscoring the occurrence and relevance of bulk phase transitions. By analyzing conductivity changes before and after two experimental runs, we inferred the thickness of the Co-rich secondary surface phase that formed during the surface transformation. Moreover, XPS and STEM analyses confirmed that the surface of the SCO catalyst underwent strontium leaching and the formation of amorphous cobalt (oxy-)hydroxide. Additionally, the thickness of the surface layer under OER conditions quantified through *operando* UV−vis spectroelectrochemistry was corroborated by the conductivity tests and STEM results. This integration not only facilitated the establishment of a robust quantitative relationship between optical density, conductivity, oxygen nonstoichiometry, and potential but also provided a reliable experimental framework for quantitatively investigating surface and bulk transformations in oxygen-deficient perovskite electrocatalysts. We envision that the proposed methodology can be coupled with additional *operando* characterization techniques, such as high-resolution thin-film X-ray diffraction, offering a powerful complementary approach to delineate the roles of dynamic surface and bulk transformations in the activity and stability of perovskite electrocatalysts.

METHODS

Thin-Film Preparation. Epitaxial $SrCoO_{2.5}$ thin films were deposited on single-crystalline (001)-orientated $(LaAlO_3)_{0.3}(SrAl_{0.5}Ta_{0.5}O_3)_{0.7}$ (LSAT) substrates through pulsed laser deposition (NanoPLD, PVD products, Inc.). A KrF excimer laser was operated with a fixed laser fluence (1.0 J cm^{-2}) and the repetition rate was 5 Hz. The growth temperature was 850 °C with 100 mTorr oxygen partial pressure. We used double-side polished LSAT substrates for the *operando* UV−vis spectroscopy measurement and a custom-made mask to deposit a 3 × 8 mm^2 $SrCoO_{2.5}$ thin film bar for *operando* conductivity measurement.

Thin-Film Characterization. The crystal structures of the thin films were characterized by high-resolution X-ray diffraction (HRXRD, Bruker D8 Discover) with monochromatic Cu $K_{\alpha 1}$ radiation and conducted in a parallel-beam geometry. X-ray reflectivity (XRR) was conducted to measure the thickness of samples. The surface chemical composition and valence state of thin films before and after the electrochemical test were obtained by using X-ray photoelectron spectroscopy (XPS, Thermo Fisher Nexsa G2) with a monochromatic Al K-alpha X-ray source. The binding energy scale of all XPS spectra has been calibrated by shifting the peak of adventitious carbon C 1s to 284.8 eV. Typically, we remove surface KOH residue on post-test samples by rinsing with deionized water multiple times before we transfer them to the analysis chamber. The cross-sectional TEM lamella was prepared by focused ion beam (FIB) milling. To avoid beam damage on the thin film surface, a protective carbon capping layer was sputtered over the surface before the milling. This procedure was found to result in negligible surface damage.[18] The atomic structure of the thin film was characterized by STEM (Thermo Scientific Spectra 300) with an acceleration voltage of 300 kV. The surface and bulk chemical composition of the sample was analyzed via a Super-X G2 EDS detector. All post-test samples for characterizations (HXRD and XPS) were taken within 30 min of the end of the electrochemical tests. Regarding the TEM measurement, the sample was promptly removed from the electrochemical cell after applying a high oxidation potential and rinsed with deionized water. It was then transferred to the FIB chamber within 10 min for TEM lamella preparation. Despite this rapid transfer, structural relaxation, evidenced by partial BM phase structures, was observed during TEM testing. Notably, more BM phase regions were detected after the sample remained in the TEM vacuum chamber for 1 day,

https://doi.org/10.1021/acsnano.4c18105
ACS Nano 2025, 19, 13999−14009

underscoring the importance of exercising caution in the TEM measurement of SCO (Figure S10).

Electrochemical Characterization. Electrochemical measurements were performed utilizing a bipotentiostat (SP-300, Biologic) within a three-electrode configuration, where the counter electrode and reference electrode were a Pt wire and a Hg/HgO electrode, respectively. Before the electrochemical test, the reference electrode was calibrated in 0.1 M KOH by the reversible hydrogen electrode (RHE, HydroFlex) with a typical value of ∼0.890 V. As for the working electrode, to enhance the electronic contact between the thin film and tantalum plate, 50 nm thick Pt was sputtered on the thin film with custom-made masks. The FFKM O-ring was applied to limit the exposure area of the thin film to the electrolyte. A spectroelectrochemical flow cell (Spectro-EFC, redox.me) was used to conduct regular electrochemical measurements and *operando* UV−vis spectroscopy experiments. A bottom magnetic mount electrochemical cell (BMM EC, redox.me) was used for *operando* conductivity measurement. All the measurements were conducted at room temperature.

***In Situ* APXPS Experiment.** APXPS experiments were conducted at the HIPPIE beamline, the MAX IV Laboratory with a photon energy of 1600 eV.[37] The electrochemical cell was connected with a manipulator and arranged with a three-electrode setup configuration. The Pt wire was a counter electrode (denoted as CE) and a leakless Ag/AgCl served as the reference electrode (RE). The working electrode (WE) consists of SCO, copper strip, and alkaline-resisting epoxy, as shown in Figure S11. Specifically, to avoid charging effects from the beginning, SCO thin film was grown on a conductive Nb:STO substrate. The sample was first coated with silver paste on its backside to make contact with a copper strip. Then, epoxy is used to encapsulate the SCO sample and the copper strip, leaving only the front side of the SCO thin film exposed. The 0.1 M KOH was degassed in a separate chamber before being moved into the XPS chamber. The beaker holder was cooled to 10 °C to lower the equilibrium vapor pressure in the chamber. All the spectra were collected under a water vapor pressure of ∼12 mbar.

***Operando* Conductivity Measurements.** The *operando* conductivity measurements were performed at room temperature, following the recommended practices by Burke *et al.*[27] The 50-nm-thick Pt contacts sputtered on the two sides of the rectangle thin film (3×8 mm^2) to configure the dual-working electrode (denoted as WE1 and WE2). The O-ring with 4.5 mm diameter was used to limit the exposure area (3×4.5 mm^2) of thin film to the electrolyte. The experiment was performed in synchronized channels mode by using a bipotentiostat equipped with an ultralow current module. WE1 was subjected to potential steps ranging from 0.94 to 1.49 V vs RHE, while WE2 applied a +10 mV offset based on the applied potentials of WE1. Then the steady-state current was measured with 10 mV offsets between WE1 and WE2 to calculate the conductivity current at different applied potentials. This calculated current difference represents the 2-fold conductance current, which is used for further conductance calculation. Given the exponential rise in OER current at higher potentials, which could potentially influence the measured conductivity current, we implemented an additional strategy within the 1.49−1.59 V potential range via alternating 5 mV steps. Initially, identical potentials were applied to both electrodes for 1 min. Subsequently, the potential on WE2 was increased by 5 mV and maintained for an additional minute. The conductance currents were extracted by calculating the difference in current response during alternating the potential steps (Figure S12).

***Operando* UV−Vis Spectroelectrochemistry Experiments.** The spectroelectrochemical flow cell was used for the *operando* UV−vis spectroscopy measurement in transmission mode. The $SrCoO_{2.5}$ thin films were deposited on double-side polished LSAT single-crystal substrates. The counter electrode, reference electrode, and electrolyte were maintained consistent with those employed in the *operando* conductivity measurements. We developed and incorporated a synchronized trigger function for spectral acquisition and electrochemical testing, ensuring the acquisition of spectra aligned with electrochemical results.[38] Before testing the thin film, we placed the bare LSAT single-crystal substrate in the cell and collected a reference spectrum while it was in contact with the electrolyte. The spectra platform consists of a deuterium-halogen light source (DH-2000-BAL, Ocean Optics) and a UV−vis spectrometer (QE Pro, Ocean Optics). The presented spectra were captured when the response current at each constant potential (Chronoamperometry, OCV to 1.59 V vs RHE) reached a steady state. The presence of bubbles made it challenging to obtain accurate spectral data at higher potentials (>1.59 V). Each spectrum was averaged for at least 1 s of data acquisition. We assumed a constant optical density of the electrolyte across the applied potential range. The optical density change (ΔOD) represents the amount of optical density change relative to the open-circuit voltage (OCV) condition.

ASSOCIATED CONTENT

Supporting Information

The Supporting Information is available free of charge at https://pubs.acs.org/doi/10.1021/acsnano.4c18105.

2θ-ω Scan and rocking curves (Figure S1); chemical capacitance and electrochemical double-layer capacitance (Figure S2); film thickness analysis (Figure S3); ratio of Sr/Co of samples (Figure S4); energy-dispersive X-ray spectroscopy distribution (Figure S5); thickness extraction of the surface and bulk layers (Figure S6); *operando* UV-vis spectra (Figure S7); optical density changes in CoO_xH_y (Figure S8); 2θ-ω scan and XRR fitting analysis (Figure S9); TEM images (Figure S10); annotated photograph of APXPS experimental setup (Figure S11); conductivity measurement (Figure S12); chemical capacitance calculation (Supporting Note 1); thickness calculation from conductivity measurement (Supporting Note 2); *operando* UV-Visible spectroelectrochemistry (Supporting Note 3); and thickness estimation from optical data analysis (Supporting Note 4) (PDF)

AUTHOR INFORMATION

Corresponding Authors

Christoph Baeumer − *MESA+ Institute for Nanotechnology, Faculty of Science and Technology, University of Twente, Enschede 7500AE, The Netherlands; Peter Gruenberg Institute and JARA-FIT, Forschungszentrum Juelich GmbH, Juelich 52425, Germany;* orcid.org/0000-0003-0008-514X; Email: c.baeumer@utwente.nl

Qiyang Lu − *School of Engineering and Research Center for Industries of the Future, Westlake University, Hangzhou, Zhejiang 310030, China;* orcid.org/0000-0002-9155-3684; Email: luqiyang@westlake.edu.cn

Authors

Yang Hu − *Zhejiang University, Hangzhou, Zhejiang 310027, China; School of Engineering, Westlake University, Hangzhou, Zhejiang 310030, China; MESA+ Institute for Nanotechnology, Faculty of Science and Technology, University of Twente, Enschede 7500AE, The Netherlands;* orcid.org/0000-0003-2731-335X

Luhan Wei − *School of Engineering, Westlake University, Hangzhou, Zhejiang 310030, China;* orcid.org/0000-0001-9639-2851

Haowen Chen − *School of Engineering, Westlake University, Hangzhou, Zhejiang 310030, China;* orcid.org/0000-0001-5318-2539

Zihan Xu − *School of Engineering, Westlake University, Hangzhou, Zhejiang 310030, China;* orcid.org/0009-0001-0564-5583

https://doi.org/10.1021/acsnano.4c18105
ACS Nano 2025, 19, 13999−14009

Andrey Shavorskiy − *MAX IV Laboratory, Lund University, Lund 22484, Sweden;* orcid.org/0000-0002-7517-5089

Complete contact information is available at: https://pubs.acs.org/10.1021/acsnano.4c18105

Notes

The authors declare no competing financial interest.

ACKNOWLEDGMENTS

This work was supported by funding from the National Natural Science Foundation of China (NSFC, Grant No. 52202148), the Research Center for Industries of the Future, and School of Engineering Dean Special Projects Fund (SOE-DSPF), Westlake University. We gratefully acknowledge support from the University of Twente in the framework of the tenure track start-up package and cofunding from the European Union (ERC, 101040669 − Interfaces at Work). Views and opinions expressed are however those of the author(s) only and do not necessarily reflect those of the European Union or the European Research Council. Neither the European Union nor the granting authority can be held responsible for them. Y.H. acknowledges support from the China Scholarship Council (award no. 202306320521). We acknowledge MAX IV Laboratory for time on HIPPIE Beamline under Proposal 20240512. Research conducted at MAX IV, a Swedish national user facility, is supported by the Swedish Research Council under contract 2018-07152, the Swedish Governmental Agency for Innovation Systems under contract 2018-04969, and Formas under contract 2019-02496. This work obtained facilities support from the Instrumentation and Service Centers for Physical Science (ISCPS) of Westlake University. The authors thank Melissa Goodwin for FIB sample preparation, Martina Tsvetanova for TEM measurement, Ellen M. Kiens, Iris C. G. van den Bosch, and Vadim Ratovskii for their support at the beamline, as well as Minh Nguyen, Tursun Abudukade, and Shreyas Harsha for help in electrode fabrication.

REFERENCES

(1) Grimaud, A.; Diaz-Morales, O.; Han, B.; Hong, W. T.; Lee, Y.-L.; Giordano, L.; Stoerzinger, K. A.; Koper, M. T. M.; Shao-Horn, Y. Activating Lattice Oxygen Redox Reactions in Metal Oxides to Catalyse Oxygen Evolution. *Nat. Chem.* **2017**, *9* (5), 457−465.

(2) Baeumer, C.; Li, J.; Lu, Q.; Liang, A. Y. L.; Jin, L.; Martins, H. P.; Duchoň, T.; Glöß, M.; Gericke, S. M.; Wohlgemuth, M. A.; Giesen, M.; Penn, E. E.; Dittmann, R.; Gunkel, F.; Waser, R.; Bajdich, M.; Nemšák, S.; Mefford, J. T.; Chueh, W. C. Tuning Electrochemically Driven Surface Transformation in Atomically Flat $LaNiO_3$ Thin Films for Enhanced Water Electrolysis. *Nat. Mater.* **2021**, *20* (5), 674−682.

(3) Kante, M. V.; Weber, M. L.; Ni, S.; van den Bosch, I. C. G.; van der Minne, E.; Heymann, L.; Falling, L. J.; Gauquelin, N.; Tsvetanova, M.; Cunha, D. M.; Koster, G.; Gunkel, F.; Nemšák, S.; Hahn, H.; Velasco Estrada, L.; Baeumer, C. A High-Entropy Oxide as High-Activity Electrocatalyst for Water Oxidation. *ACS Nano* **2023**, *17* (6), 5329−5339.

(4) Marelli, E.; Gazquez, J.; Poghosyan, E.; Müller, E.; Gawryluk, D. J.; Pomjakushina, E.; Sheptyakov, D.; Piamonteze, C.; Aegerter, D.; Schmidt, T. J.; Medarde, M.; Fabbri, E. Correlation between Oxygen Vacancies and Oxygen Evolution Reaction Activity for a Model Electrode: $PrBaCo_2O_{5+\delta}$. *Angew. Chemie - Int. Ed.* **2021**, *60* (26), 14609−14619.

(5) Choi, M.-J.; Wang, L.; Stoerzinger, K. A.; Chung, S.-Y.; Chambers, S. A.; Du, Y. Epitaxial Design of Complex Nickelates as Electrocatalysts for the Oxygen Evolution Reaction. *Adv. Energy Mater.* **2023**, *13* (22), No. 2300239.

(6) Zhang, Y.; Liu, J.; Xu, Y.; Xie, C.; Wang, S.; Yao, X. Design and Regulation of Defective Electrocatalysts. *Chem. Soc. Rev.* **2024**, *53* (21), 10620−10659.

(7) Kiens, E. M.; Choi, M.-J.; Wei, L.; Lu, Q.; Wang, L.; Baeumer, C. Deeper Mechanistic Insights into Epitaxial Nickelate Electrocatalysts for the Oxygen Evolution Reaction. *Chem. Commun.* **2023**, *59*, 4562.

(8) Bosse, J.; Gu, J.; Choi, J.; Roddatis, V.; Zhuang, Y.-B.; Kani, N. A.; Hartl, A.; Garcia-Fernandez, M.; Zhou, K.-J.; Nicolaou, A.; Lippert, T.; Cheng, J.; Akbashev, A. R. Molecular O_2 Dimers and Lattice Instability in a Perovskite Electrocatalyst. *J. Am. Chem. Soc.* **2024**, *146* (34), 23989−23997.

(9) Weber, M. L.; Lole, G.; Kormanyos, A.; Schwiers, A.; Heymann, L.; Speck, F. D.; Meyer, T.; Dittmann, R.; Cherevko, S.; Jooss, C.; Baeumer, C.; Gunkel, F. Atomistic Insights into Activation and Degradation of $La_{0.6}Sr_{0.4}CoO_{3-\Delta}$ Electrocatalysts under Oxygen Evolution Conditions. *J. Am. Chem. Soc.* **2022**, *144* (39), 17966−17979.

(10) Lu, N.; Zhang, P.; Zhang, Q.; Qiao, R.; He, Q.; Li, H. B.; Wang, Y.; Guo, J.; Zhang, D.; Duan, Z.; Li, Z.; Wang, M.; Yang, S.; Yan, M.; Arenholz, E.; Zhou, S.; Yang, W.; Gu, L.; Nan, C. W.; Wu, J.; Tokura, Y.; Yu, P. Electric-Field Control of Tri-State Phase Transformation with a Selective Dual-Ion Switch. *Nature* **2017**, *546* (7656), 124−128.

(11) Lu, Q.; Yildiz, B. Voltage-Controlled Topotactic Phase Transition in Thin-Film $SrCoO_x$ Monitored by *in Situ* X-Ray Diffraction. *Nano Lett.* **2016**, *16* (2), 1186−1193.

(12) Chen, H.; Xu, Z.; Wei, L.; Dong, M.; Hu, Y.; Lu, Y.; Zhang, N.; Wu, J.; Lu, Q. Manipulating Protons and Oxygen Vacancies in Nickelate Oxides via Thermochemical Dehydration. *J. Mater. Chem. A* **2024**, *12*, 23658−23669.

(13) Anand, S.; Toriyama, M. Y.; Wolverton, C.; Haile, S. M.; Snyder, G. J. A Convergent Understanding of Charged Defects. *Accounts Mater. Res.* **2022**, *3* (7), 685−696.

(14) Maier, J. Complex Oxides: High Temperature Defect Chemistry vs. Low Temperature Defect Chemistry. *Phys. Chem. Chem. Phys.* **2003**, *5* (11), 2164−2173.

(15) Yang, K.; Lu, Y.; Hu, Y.; Xu, Z.; Zheng, J.; Chen, H.; Wang, J.; Yu, Y.; Zhang, H.; Liu, Z.; Lu, Q. Differentiating Oxygen Exchange Reaction Mechanisms across Phase Boundaries. *J. Am. Chem. Soc.* **2023**, *145* (47), 25806−25814.

(16) Fabbri, E.; Nachtegaal, M.; Binninger, T.; Cheng, X.; Kim, B.-J.; Durst, J.; Bozza, F.; Graule, T.; Schäublin, R.; Wiles, L.; Pertoso, M.; Danilovic, N.; Ayers, K. E.; Schmidt, T. J. Dynamic Surface Self-Reconstruction Is the Key of Highly Active Perovskite Nano-Electrocatalysts for Water Splitting. *Nat. Mater.* **2017**, *16* (9), 925−931.

(17) Li, H.; Chen, Y.; Seow, J. Z. Y.; Liu, C.; Fisher, A. C.; Ager, J. W.; Xu, Z. J. Surface Reconstruction of Perovskites for Water Oxidation: The Role of Initial Oxides' Bulk Chemistry. *Small Sci.* **2022**, *2* (1), No. 2100048.

(18) Füngerlings, A.; Wohlgemuth, M.; Antipin, D.; van der Minne, E.; Kiens, E. M.; Villalobos, J.; Risch, M.; Gunkel, F.; Pentcheva, R.; Baeumer, C. Crystal-Facet-Dependent Surface Transformation Dictates the Oxygen Evolution Reaction Activity in Lanthanum Nickelate. *Nat. Commun.* **2023**, *14* (1), 8284.

(19) Wu, Y.-H.; Janák, M.; Abdala, P. M.; Borca, C. N.; Wach, A.; Kierzkowska, A.; Donat, F.; Huthwelker, T.; Kuznetsov, D. A.; Müller, C. R. Probing Surface Transformations of Lanthanum Nickelate Electrocatalysts during Oxygen Evolution Reaction. *J. Am. Chem. Soc.* **2024**, *146* (17), 11887−11896.

(20) Nemudry, A.; Rudolf, P.; Schöllhorn, R. Topotactic Electrochemical Redox Reactions of the Defect Perovskite $SrCoO_{2.5+x}$. *Chem. Mater.* **1996**, *8* (9), 2232−2238.

(21) Jeen, H.; Choi, W. S.; Freeland, J. W.; Ohta, H.; Jung, C. U.; Lee, H. N. Topotactic Phase Transformation of the Brownmillerite $SrCoO_{2.5}$ to the Perovskite $SrCoO_{3-\delta}$. *Adv. Mater.* **2013**, *25* (27), 3651−3656.

(22) Lu, Q.; Chen, Y.; Bluhm, H.; Yildiz, B. Electronic Structure Evolution of $SrCoO_x$ during Electrochemically Driven Phase

Transition Probed by *in Situ* X-Ray Spectroscopy. *J. Phys. Chem. C* **2016**, *120* (42), 24148−24157.
(23) Petrie, J. R.; Jeen, H.; Barron, S. C.; Meyer, T. L.; Lee, H. N. Enhancing Perovskite Electrocatalysis through Strain Tuning of the Oxygen Deficiency. *J. Am. Chem. Soc.* **2016**, *138* (23), 7252−7255.
(24) Hu, S.; Han, W.; Hu, S.; Seidel, J.; Wang, J.; Wu, R.; Wang, J.; Zhao, J.; Xu, Z.; Ye, M.; Chen, L. Voltage-Controlled Oxygen Non-Stoichiometry in $SrCoO_{3-\delta}$ Thin Films. *Chem. Mater.* **2019**, *31* (16), 6117−6123.
(25) Oyama, G.; Yamada, Y.; Natsui, R. I.; Nishimura, S. I.; Yamada, A. Kinetics of Nucleation and Growth in Two-Phase Electrochemical Reaction of Li_XFePO_4. *J. Phys. Chem. C* **2012**, *116* (13), 7306−7311.
(26) Le Toquin, R.; Paulus, W.; Cousson, A.; Prestipino, C.; Lamberti, C. Time-Resolved in Situ Studies of Oxygen Intercalation into $SrCoO_{2.5}$, Performed by Neutron Diffraction and X-Ray Absorption Spectroscopy. *J. Am. Chem. Soc.* **2006**, *128* (40), 13161−13174.
(27) Burke, M. S.; Kast, M. G.; Trotochaud, L.; Smith, A. M.; Boettcher, S. W. Cobalt-Iron (Oxy)Hydroxide Oxygen Evolution Electrocatalysts: The Role of Structure and Composition on Activity, Stability, and Mechanism. *J. Am. Chem. Soc.* **2015**, *137* (10), 3638−3648.
(28) Burke, M. S.; Enman, L. J.; Batchellor, A. S.; Zou, S.; Boettcher, S. W. Oxygen Evolution Reaction Electrocatalysis on Transition Metal Oxides and (Oxy)Hydroxides: Activity Trends and Design Principles. *Chem. Mater.* **2015**, *27* (22), 7549−7558.
(29) Biesinger, M. C.; Payne, B. P.; Grosvenor, A. P.; Lau, L. W. M.; Gerson, A. R.; Smart, R. S. C. Resolving Surface Chemical States in XPS Analysis of First Row Transition Metals, Oxides and Hydroxides: Cr, Mn, Fe, Co and Ni. *Appl. Surf. Sci.* **2011**, *257* (7), 2717−2730.
(30) Lu, Q. How to Correctly Analyze 2*p* X-Ray Photoelectron Spectra of 3*d* Transition-Metal Oxides: Pitfalls and Principles. *ACS Nano* **2024**, *18* (22), 13973−13982.
(31) Favaro, M.; Yang, J.; Nappini, S.; Magnano, E.; Toma, F. M.; Crumlin, E. J.; Yano, J.; Sharp, I. D. Understanding the Oxygen Evolution Reaction Mechanism on CoO_x Using *Operando* Ambient-Pressure X-Ray Photoelectron Spectroscopy. *J. Am. Chem. Soc.* **2017**, *139* (26), 8960−8970.
(32) Boucly, A.; Artiglia, L.; Fabbri, E.; Palagin, D.; Aegerter, D.; Pergolesi, D.; Novotny, Z.; Comini, N.; Diulus, J. T.; Huthwelker, T.; Ammann, M.; Schmidt, T. J. Direct Evidence of Cobalt Oxyhydroxide Formation on a $La_{0.2}Sr_{0.8}CoO_3$ Perovskite Water Splitting Catalyst. *J. Mater. Chem. A* **2022**, *10* (5), 2434−2444.
(33) Koohfar, S.; Ghasemi, M.; Hafen, T.; Dimitrakopoulos, G.; Kim, D.; Pike, J.; Elangovan, S.; Gomez, E. D.; Yildiz, B. Improvement of Oxygen Reduction Activity and Stability on a Perovskite Oxide Surface by Electrochemical Potential. *Nat. Commun.* **2023**, *14* (1), 7203.
(34) Wang, S.; Jiang, Q.; Ju, S.; Hsu, C.-S.; Chen, H. M.; Zhang, D.; Song, F. Identifying the Geometric Catalytic Active Sites of Crystalline Cobalt Oxyhydroxides for Oxygen Evolution Reaction. *Nat. Commun.* **2022**, *13* (1), 6650.
(35) Wu, T.; Sun, S.; Song, J.; Xi, S.; Du, Y.; Chen, B.; Sasangka, W. A.; Liao, H.; Gan, C. L.; Scherer, G. G.; Zeng, L.; Wang, H.; Li, H.; Grimaud, A.; Xu, Z. J. Iron-Facilitated Dynamic Active-Site Generation on Spinel $CoAl_2O_4$ with Self-Termination of Surface Reconstruction for Water Oxidation. *Nat. Catal.* **2019**, *2* (9), 763−772.
(36) Mefford, J. T.; Akbashev, A. R.; Kang, M.; Bentley, C. L.; Gent, W. E.; Deng, H. D.; Alsem, D. H.; Yu, Y. S.; Salmon, N. J.; Shapiro, D. A.; Unwin, P. R.; Chueh, W. C. Correlative *Operando* Microscopy of Oxygen Evolution Electrocatalysts. *Nature* **2021**, *593* (7857), 67−73.
(37) Zhu, S.; Scardamaglia, M.; Kundsen, J.; Sankari, R.; Tarawneh, H.; Temperton, R.; Pickworth, L.; Cavalca, F.; Wang, C.; Tissot, H.; Weissenrieder, J.; Hagman, B.; Gustafson, J.; Kaya, S.; Lindgren, F.; Kallquist, I.; Maibach, J.; Hahlin, M.; Boix, V.; Gallo, T.; Rehman, F.; D'Acunto, G.; Schnadta, J.; Shavorskiy, A. HIPPIE: A New Platform for Ambient-Pressure X-Ray Photoelectron Spectroscopy at the MAX IV Laboratory. *J. Synchrotron Radiat.* **2021**, *28*, 624−636.
(38) Wei, L.; Hu, Y.; Huang, Y.; Lu, Y.; Xu, Z.; Zhang, N.; Lu, Q. Deconvoluting Surface and Bulk Charge Storage Processes in Redox-Active Oxides by Integrating Electrochemical and Optical Insights. *J. Am. Chem. Soc.* **2024**, *146* (34), 24167−24176.

https://doi.org/10.1021/acsnano.4c18105
ACS Nano 2025, 19, 13999−14009